PHOTONICS Research

Generation of wavelength-tunable and coherent dual-wavelength solitons in the C + L band by controlling the intracavity loss

Tianyu Zhu,[1] Zhaokun Wang,[1,2] D. N. Wang,[1,3] Fan Yang,[1] and Liujiang Li[1]

[1]College of Optical and Electronic Technology, China Jiliang University, Hangzhou 310018, China
[2]e-mail: 16a0402091@cjlu.edu.cn
[3]e-mail: dnwang@cjlu.edu.cn

Received 26 March 2019; revised 22 May 2019; accepted 9 June 2019; posted 10 June 2019 (Doc. ID 363412); published 18 July 2019

A wavelength-tunable and dual-wavelength mode-locking operation is achieved in an Er-doped fiber laser using a hybrid no-core fiber graded index multimode fiber as the saturable absorber. In the tuning operation, continuously wavelength-tunable pulses with a tuning range of 46.7 nm, stable 3-dB bandwidth of around 5 nm, and pulse duration of ~850 fs are obtained by increasing the intracavity loss of a variable optical attenuator. In the dual-wavelength operation, the two solitons at different wavelengths demonstrate the characteristics of mutual coherence. By increasing the intracavity loss, the spectral spacing can be tuned from 11 to 33.01 nm while maintaining the coherence of the solitons. Such coherent solitons have high potential for applications in dual-comb frequency and multicolor pulses in nonlinear microscopy.

https://doi.org/10.1364/PRJ.7.000853

1. INTRODUCTION

Wavelength-tunable and dual-wavelength mode-locking Er-doped fiber (EDF) lasers operated in the telecom band have versatile applications in wavelength division multiplexing, optical signal processing, optical sensing, and precision spectroscopy [1–3]. Until now, several methods have been proposed for broadband wavelength tuning and multiwavelength operation, including conventional bandpass filters, tunable interference filters [4–8], self-frequency shift [9], intracavity birefringence adjustment [10], intracavity loss control [11,12], and so on. For a wavelength-tunable mode-locking operation, the tuning range is limited by the loss/gain distribution band of the Er-doped gain fiber. Thus, the relatively wide tuning range that covers the C + L band is difficult to achieve. The loss/gain distribution is affected by the insertion loss of the cavity and the length of the EDF. The precise control of the additional intracavity loss is an efficient method to change the population inversion in the fiber cavity and achieve broadband wavelength tuning [13]. The dual-wavelength Er-doped passively mode-locked fiber lasers can yield double-pulse trains with different central wavelengths simultaneously. Theoretically, the laser spectrum can possess two peaks with similar gain under certain pump and signal conditions, considering the gain spectral profile of the Er-doped gain fiber. However, the strong mode competition in the homogeneously broadened gain medium may hinder the stable output of a dual-wavelength fiber laser [14]. Similarly, the tuning of the cavity loss can be applied for dual-wavelength output by balancing the mode competition and improving the gain spectral profile. Zhao *et al.* [12] report a switchable dual-wavelength Er-doped passively mode-locked ultrafast fiber laser with subpicosecond pulse output at both the wavelengths 1532 and 1557 nm just by varying the intracavity loss with a tunable attenuator. In some cases, the dual solitons at different central wavelengths have similar parameters, including intracavity pulse energy, pulse duration, polarization state, etc., which indicate the mutual coherence of the two solitons. This coherence is a decisive parameter for the application of coherent pulse synthesis, dual-comb frequency, and so on. Although the coherence of dissipative solitons (DSs) and Raman dissipative solitons (RDSs) has been proved previously [15,16], the coherent characteristics of conventional solitons have not yet been observed.

So far, a number of saturable absorbers (SAs) have been reported for the generation of wavelength-tunable dual-wavelength in mode-locked fiber lasers, including nonlinear polarization rotation (NPR) [6–9], single-wall carbon nanotubes (CNTs) [17,18], nonlinear optical loop mirrors (NOLMs) [14,19,20], semiconductor SA mirrors (SESAMs) [4,21], graphene [5,10], black phosphorus (BP) [22], molybdenum disulphide (e.g., WS_2 [23]), etc. In our previous works, a new type of all-fiber SA based on the nonlinear multimode interference of the graded index multimode fiber (GIMF) was proposed and demonstrated [24–26]. The light intensity-dependent self-focusing length is caused by the nonlinear multimode interference in GIMF, and the core diameter mismatch

from the GIMF to the single-mode fiber (SMF) provides the light intensity-dependent transmission. The all-fiber structure gives the advantages of a very small insertion loss and a high damage threshold [27]. Moreover, such an SA supports various types of soliton outputs, including tunable bound solitons [28], stretched pulses [29], 1.0 μm DS pulses [30], etc. Although the switchable mode-locking operation was obtained by stretching of the GIMF SA, further prospective studies on the tunable and multiwavelength solitons are still required.

In this paper, based on net-anomalous-dispersion Er-doped laser with the all-fiber no-core fiber (NCF)-GIMF SA, a widely tunable mode-locking operating in the C + L band is achieved by changing the additional intracavity loss. The tunable central wavelength is tuned from 1602.6 to 1555.9 nm in a range of 46.7 nm. Furthermore, by properly adjusting the polarization controller (PC), a mode-locked pulse of the coherent dual wavelength is generated. An interference pattern is observed in the autocorrelation trace of the dual solitons in an anomalous mode-locked fiber laser for the first time, which indicates the mutual coherence of the dual-wavelength solitons. The spectral separation between the two coherent solitons ranging from 11 to 33.01 nm is tuned by increasing the intracavity loss. And the energy of the two wavelengths can also be switched by slightly adjusting the PC.

2. EXPERIMENTAL RESULTS

A. Loss Control Performance of the Commercial VOA

The chosen variable optical attenuator (VOA) device in the experiment is a 1550 nm commercial mini-type manual variable attenuator (Advanced Fiber Resources). The additional intracavity loss control range is from 0 to 30 dB, which can be adjusted by rotating the screw on the VOA. Before the formal experiment, a fine calibration is implemented; then by slightly rotating the screw, the insertion loss of the VOA as a function of the rotated number (every quarter circle) is recorded. During the formal experiment, these data are used directly. In order to test its operation performance, an Er-doped amplified spontaneous emission (ASE) laser is constructed, which consists of a ~2 m long standard single-mode Er-doped gain fiber (Nufern SM-ESF-7/125). Figure 1(a) shows the intensity of the ASE gain spectrum at the pump power of 80 mW. The peak emission is centered at 1556 nm. The gain tilt at above 1556 nm is invariable, and there is a distinct turning point at 1575 nm. Figure 1(b) shows the varied intensity difference of the ASE transmission spectrum (VOA device) with the increase of the additional intracavity loss by using a 1550 nm commercial broadband light source (BBS) (Amonics). The corresponding transmission intensity difference curves at different insertion losses are obtained by subtracting the decreasing transmission ASE spectrum from the 0-dB-insertion-loss transmission ASE spectrum, as shown in Fig. 1(b). It can be seen from the figure that there is a decreasing trend in the intensity difference, and the flat curve indicates that the VOA device has no wavelength selectivity.

Generally, the threshold of population inversion in laser operation which determines the gain threshold at different wavelengths can be influenced by the intracavity loss of the fiber laser, the length and the dopant concentration of the EDF. Because the gain in the L-band is much lower than the gain threshold in the C-band, EDF laser emission in the L-band could be difficult [31]. According to Ref. [19], in a laser resonator, a low loss of the cavity and a relatively long EDF ensure a low threshold of population inversion, which leads to a low gain threshold. It means that a low loss cavity can support the laser emission in the L-band. Then by increasing the intracavity loss, the lasing wavelength can move to the C-band to balance the change in gain value.

B. Characterizations of a Hybrid Multimode Optical Fiber SA

The SA is fabricated by sequentially fusing splicing of an SMF, an NCF of ~181 μm, a GIMF (62.5/125, Corning) of ~27.5 cm, and an SMF, as shown in Fig. 2(a). The lengths of the NCF and GIMF are not intentionally chosen. However, the length of NCF cannot be too long, in order to guarantee the small insertion loss of the NCF-GIMF device. The red arrow in Fig. 2(a) represents the path of light in the SA structure. The introduction of the NCF is used to expand the mode field diameter at the entrance of the GIMF, which can improve the saturable absorption property and suppress the power leakage into the radiation and cladding modes [28]. As shown in Fig. 2(b), the nonlinear saturable absorption curve exhibits typical characteristics of saturable absorption. The modulation depth, saturation intensity, and nonlinear loss of the SA are measured as 4.57%, 1.92 μJ/cm^2, and

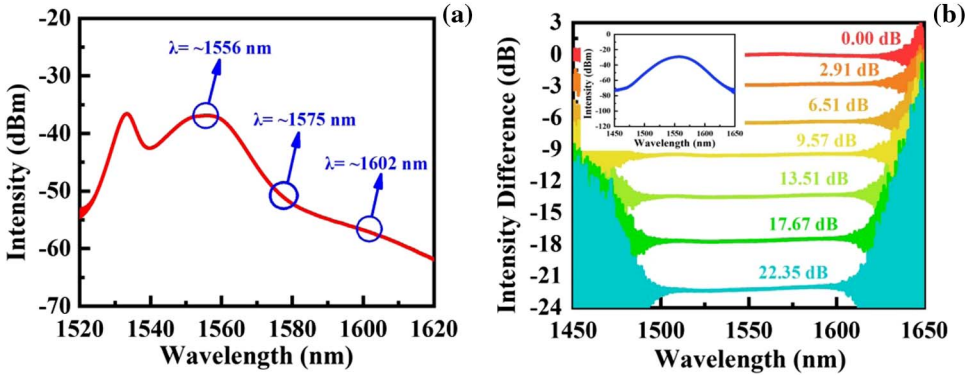

Fig. 1. (a) ASE transmission spectrum of the EDF; (b) varied intensity differences of the ASE transmission spectrum (VOA device) with the increase of the additional intracavity loss (labeled); inset, the original spectrum of the BBS.

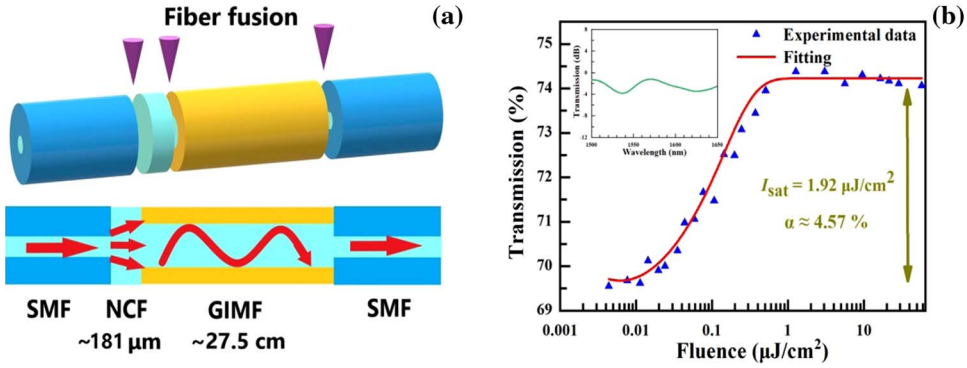

Fig. 2. (a) Schematic diagram of SMF-NCF-GIMF-SMF structure; (b) nonlinear saturable absorption curve of the NCF-GIMF device; inset, the transmission spectrum of the NCF-GIMF device.

~69.71%, respectively. As shown in the inset of Fig. 2(b), the insertion loss of the device with a relatively flat transmission curve is smaller than 4 dB, which ensures a small influence on the original laser emission wavelength of the fiber laser. Compared with other SAs, the NCF-GIMF device has the advantages of versatility, simplicity, and excellent mechanical performance.

C. Experimental Setup

The schematic diagram of the tunable and dual-wavelength passively mode-locked EDF laser with the SA based on an NCF-GIMF device is shown in Fig. 3. The 1480 nm forward pumping light enters the fiber ring cavity via a 1480 nm polarization-independent isolator (PI-ISO) and a 1480/1550 nm wavelength division multiplexer (WDM). The laser propagates counterclockwise in the ring cavity. This cavity consists of a WDM, the standard single mode erbium-doped gain fiber (Nufern SM-ESF-7/125), a 1550 nm PI-ISO, a 90:10 optical coupler (OC) with 10% output, the SA fixed on a stretcher with a precision of approximately 10 μm, a PC, and a VOA device. The inset in Fig. 3 is a picture of the VOA, where the orange arrow refers to the direction of increasing the insertion loss. The SMF with the dispersion coefficient of 18 ps/(nm · km) and the EDF with the dispersion coefficient

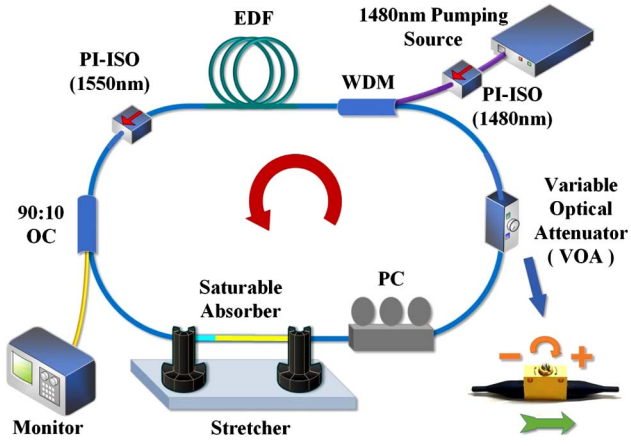

Fig. 3. Schematic diagram of the experimental setup. The red arrow represents the laser direction.

of −46.25 ps/(nm · km) used in the cavity are ~11 and ~2 m, respectively. Thus, the overall net anomalous dispersion is calculated to be around −0.149 ps^2. The PI-ISO (1550 nm) is used to ensure the directional operation of the laser. The PC is included for fine adjustment of the birefringence and optimization of the mode-locking operation. The characteristics of the output pulses can be obtained by use of an optical spectrum analyzer (OSA) (Yokogawa, AQ6370D) with 0.02 nm resolution, a 1 GHz digital oscilloscope (Tektronix, TDS5104B), a 9 kHz–3.2 GHz radio frequency (RF) spectrum analyzer (Siglent, SSA3032X), a 5 GHz photodetector (Thorlabs, DET08CFC/M), and a second-harmonic autocorrelator (APE, PulseCheck 150), simultaneously.

D. Wavelength Tuning in the C + L Band

When the pump power is set to ~252 mW and the VOA is set to 0 dB, the conventional solitons are generated by appropriately adjusting the PC; the corresponding output characteristics are displayed in Fig. 4. Figure 4(a) shows a typical traditional soliton pulse spectrum with the central wavelength of ~1602.6 nm and a 3 dB bandwidth of ~4.94 nm. The appearance of Kelly sidebands in the pulse spectrum exhibits a clear anomalous dispersion soliton state, and the asymmetric basement of the optical spectrum results from the oscillating at the right edge of the gain range. The small loss of the cavity and the large gain provided by the long EDF guarantee the low population inversion, which is beneficial for the oscillation at 1.6 μm [11]. However, due to the strong mode competition in the homogeneously broadened gain medium and relatively higher transmission of the NCF-GIMF device within the 1565–1570 nm bandwidth, continuous wave (CW) coexists at the wavelength of ~1570 nm. Figure 4(b) is the corresponding autocorrelation trace, which indicates a pulse width of ~816 fs by a sech^2 pulse profile. Thus, the time-bandwidth product (TBP) is ~0.328 (larger than the standard TBP of 0.315), which indicates a small chirp of the pulse. The measured pulse train in Fig. 4(c) is ~60.4 ns, which is in accordance with the fundamental repetition frequency of 16.56 MHz in Fig. 4(d) and reveals its single-pulse operation state. In Fig. 4(d), the signal-to-noise ratio (SNR) at the fundamental repetition frequency is ~56 dB, with 10 Hz resolution bandwidth (RBW) and 18 MHz span, and the inset

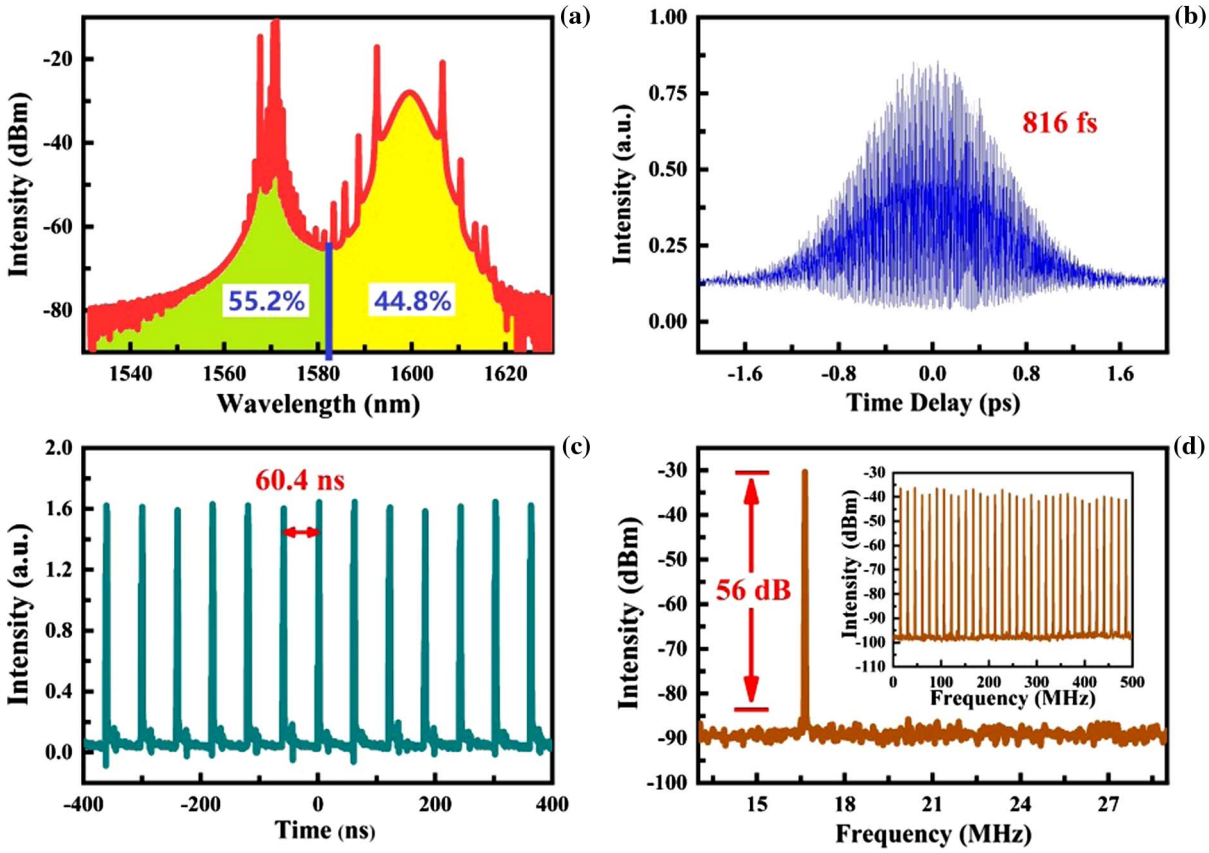

Fig. 4. Conventional mode-locked single soliton outputs. (a) Optical spectrum; (b) autocorrelation trace; (c) pulse train; (d) RF spectrum.

represents the RF spectrum over a frequency range of 500 MHz. To remove the CW energy from calculation, we use the integration method. When the pump power is 252 mW and the insertion loss is 0 dB, the average power is measured to be 4.26 mW. As shown in Fig. 4(a), the average power of mode locking has the proportion of ~44.8%. So the average power of mode locking is taken as 1.91 mW, and the corresponding pulse energy is calculated to be 111.46 pJ by removing the continuous light energy at 1570 nm. All the results obtained indicate a good performance of mode-locked laser operation. The stability test of the laser system lasted for over 24 h, and it was found that the output spectrum, pulse width, output power, and repetition rate are quite stable.

The evolution of the output power versus pump power is measured; the results obtained are shown in Fig. 5. The self-started mode-locking threshold of the pump power is measured to be 139.2 mW, and the mode-locking operation can be maintained when the pump power is decreased to ~50 mW due to the pump hysteresis effect. By enhancing the pump power, the output power increases linearly with a slope of 2%. As the pump power increases, the output pulses keep the fundamental frequency state, and the pulse width does not change significantly. The output power reaches 5.69 mW at the maximum pump power of 275 mW, and the corresponding pulse energy is calculated to be 64.6 pJ by removing the continuous light energy at 1570 nm. It can be seen from Fig. 5 that the pulse energy at the maximum pump power is smaller than the pulse energy of 111.46 pJ at ~252 mW, as the energy proportion of the CW light at ~275 mW is much larger than that at ~252 mW. Benefiting from the all-fiber structure, the SA device demonstrates good induced thermal damage, and the mode-locked fiber laser can support ultrafast pulse generation with higher single optical pulse energy output.

With the increase of the additional intracavity loss from 0 to 16.69 dB by adjusting the VOA, the central wavelength of the fundamental solitons is tuned from 1602.6 to 1555.9 nm in a continuous manner, as shown in Fig. 6. It can be seen that the

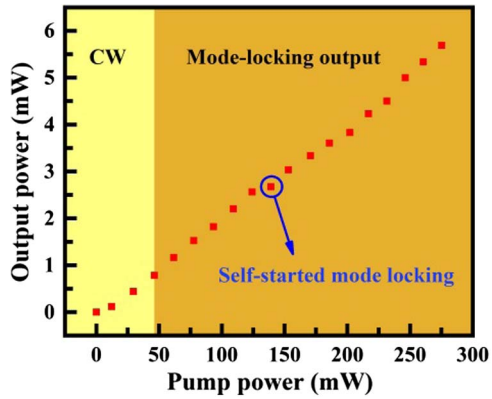

Fig. 5. Output power of the fiber laser versus pump power.

general tendency is a shift toward shorter wavelengths with the increase of the additional losses. This evolution is well explained by the population inversion theory, which demonstrates the value of the population inversion at the threshold directly influencing the emitting wavelength [11]. The increase of the total-cavity loss promotes the threshold population inversion, which determines the corresponding blueshift of the gain-maximum position. A 46.7 nm tuning range essentially covers the emission spectrum of the EDF. During the tuning process, the PC keeps its orientation, and the pump power is also maintained. When the mode-locking laser operates in the region of the L-band, the CW light at 1570 nm cannot be eliminated, as shown in Figs. 6(a)–6(d). In contrast, the CW light no longer exists in the C-band tuning range, as shown in Figs. 6(e)–6(k). This means that there is not enough gain at 1570 nm to compensate for the losses. Unfortunately, when the additional intracavity loss in the cavity exceeds 22.76 dB, the excessive loss destroys the mode-locking operation. It should be noted that the tuning process can be completely reversible. When the additional intracavity loss is decreasing, the wavelength can be tuned back to the initial value.

In Fig. 7, we summarize the various characteristics of the tunable mode-locking operation at the pump power of 252 mW. As shown in Fig. 7(a), with the additional intracavity loss varying from 0 to 16.69 dB, the wavelength experiences a blueshift. Note that the operating wavelength demonstrates a different evolution trend in different wavelength ranges with the adjustment of the additional intracavity loss. When the wavelength is larger than 1575 nm, a sharp slope of −59.2 nm/dB is applied, which is attributed to the relatively flat ASE spectrum in this wavelength region. The slope decreases to −1.16 nm/dB in the rest of the tuning region, due to the increase of the gain slope. Similarly, there is also an obvious turning point at 1575 nm in the evolution of the average power and the single-pulse energy, as shown in Fig. 7(b). With the tuning of the wavelength, the single-pulse energy is increased from 111 to 365 pJ and then decreased to 28 pJ. The average power after subtracting the CW light demonstrates the same trend. The temporary increase of pulse energy is caused by the higher gain level in the C-band compared with that in the L-band. According to Fig. 7(c), the pulse width keeps around 800 fs, and the 3-dB bandwidth of the spectra is ∼5 nm, both of which are essentially unchanged as the central wavelength of the soliton is tuned.

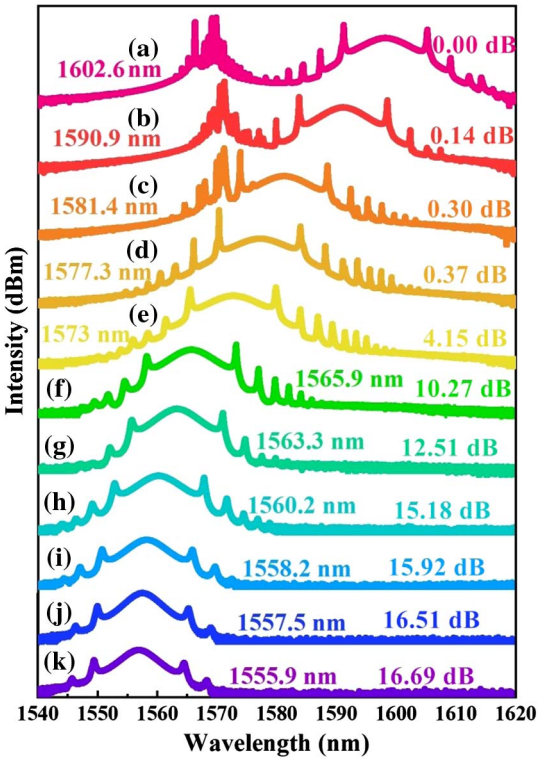

Fig. 6. (a)–(k) Tunable spectra of the mode-locking operation in the C + L band at different additional insertion losses.

E. Coherent Dual-Wavelength Soliton with Controllable Spacing

As previously mentioned, there is a strong cluster of CW light centered at ∼1570 nm accompanied by the mode-locking solitons when the additional intracavity loss introduced by the VOA is small. The adequate gain value at 1565 and 1600 nm could be satisfied simultaneously, which makes the dual-wavelength mode-locked output possible. By finely rotating the PC into the condition that the CW laser and the mode-locked pulse coexist in the cavity and the additional loss of VOA is 0 dB, the CW laser at 1570 nm can turn into the mode-locking regime, and the dual-wavelength mode-locked operation appears, as shown in Fig. 8(a). It can be seen from Fig. 8(a) that there are two mode-locking spectral components centered at 1569.63 and 1602.64 nm, respectively. The 3-dB bandwidths are ∼3.5 and 4.3 nm, respectively, with a wavelength spacing of 33.01 nm. In the dual-wavelength operation, the output power is measured to be 5.04 mW, corresponding to 2.67 mW at 1569.63 nm and 2.37 mW at 1602.64 nm. It is too difficult to separate these two closely spaced wavelengths due to the absence of an effective spectral filter. Figure 8(a1) shows the autocorrelation trace of the dual solitons, and a unique interference envelope is obtained, indicating the high mutual coherence of the solitons. Although the dual solitons have the comb-shaped autocorrelation curve, they are also different from one-color (that is, of the same spectrum) bound solitons based on Kerr nonlinearity. In our case, the dual solitons are synthesized into a single pulse in the measuring process owing to the mutual coherence of the two solitons. The interval between fringes is 0.442 ps, corresponding to the spectral spacing between the two solitons of different wavelengths. And the width of the individual fringe is much smaller than that of the single soliton, as is defined by the whole spectral range of the dual solitonic complex. The full width at half-maximum (FWHM) of the ACF is equal to 980 fs. It is worth noting that the relatively high fringe visibility demonstrates that the dual-wavelength conventional solitons are in efficient coherence.

Benefiting from the change of the intracavity loss/gain distribution introduced by the adjustment of the VOA, the wavelength spacing of the two solitons with nearly equal magnitude can be continuously tuned by adjusting the additional insertion slightly. Figures 8(a)–8(e) represent different spectra of the dual wavelength with spectral spacing tuning from 33.01 to 11 nm

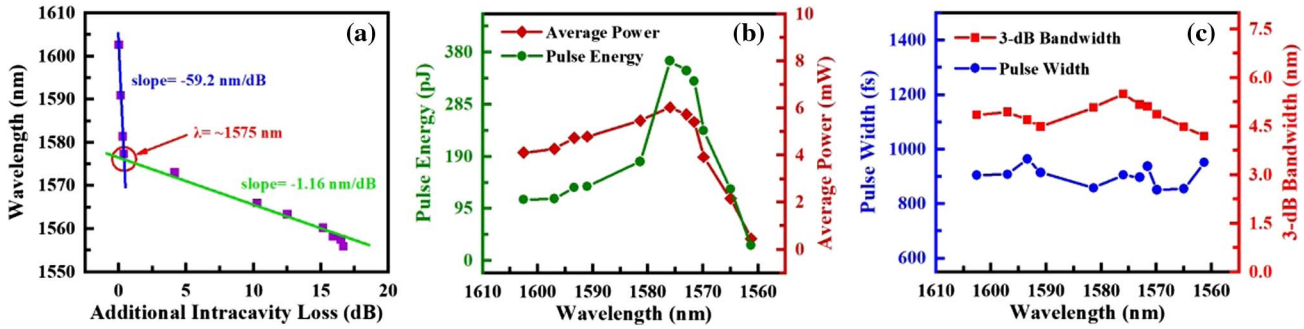

Fig. 7. Evolution of relevant parameters during tuning process. (a) Corresponding central wavelengths at different intracavity losses; (b) pulse energy and average power after subtracting the CW light as functions of the tuning wavelength; (c) pulse width and 3-dB bandwidth as functions of the tuning wavelength.

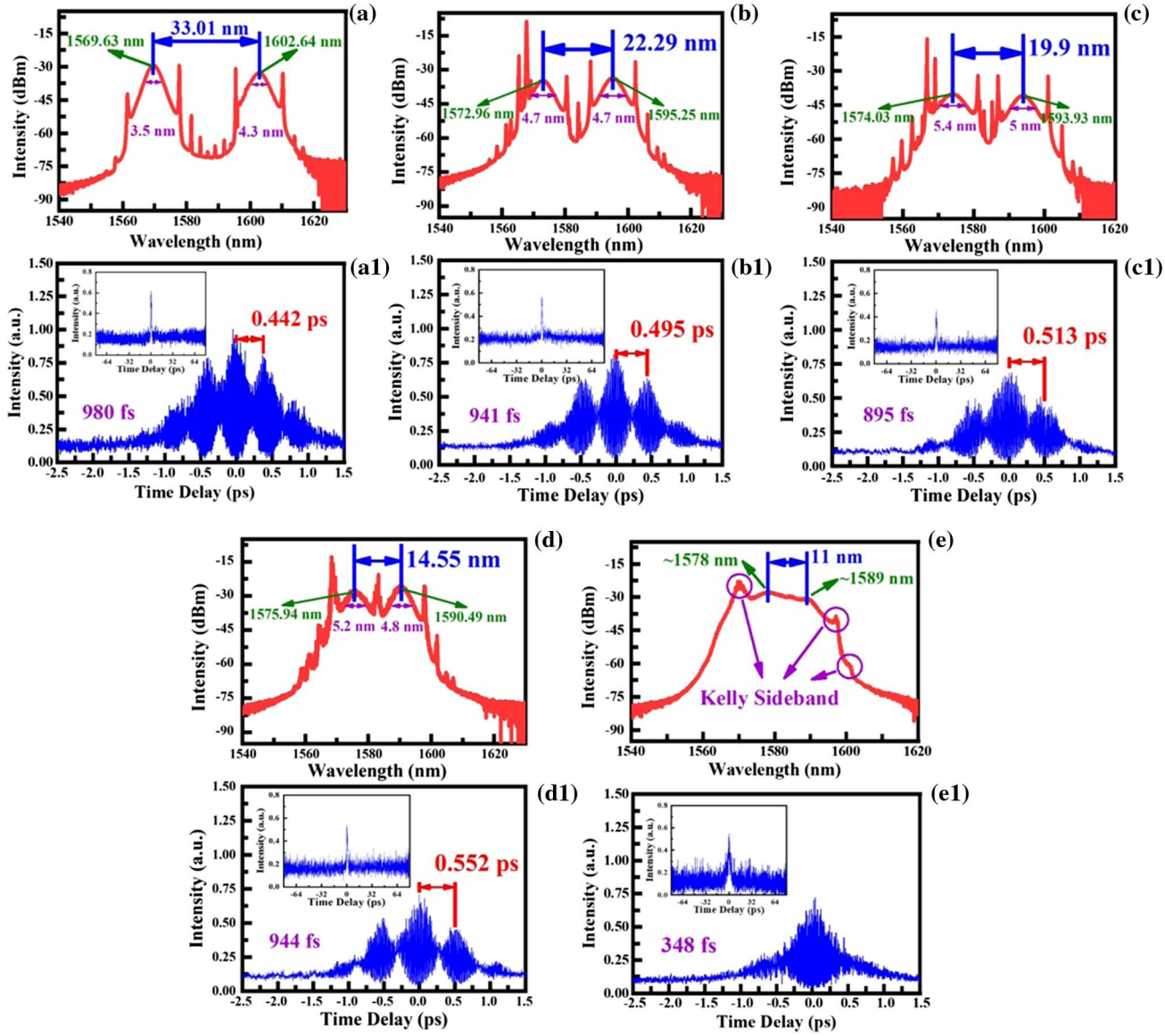

Fig. 8. (a)–(e) Different spectra of dual wavelength; (a1)–(e1) corresponding autocorrelation traces; insets: wide-range autocorrelation trace diagram.

Table 1. Detailed Characteristics of the Coherent Dual-Wavelength Solitons Corresponding to Fig. 8[a]

F. N.	S. S.	C. W.	B. W.	M. P.	P. W.
Figures 8(a) and 8(a1)	33.01 nm	1569.63; 1602.64 nm	3.5; 4.3 nm	0.442 ps	980 fs
Figures 8(b) and 8(b1)	22.29 nm	1572.96; 1595.25 nm	4.7; 4.7 nm	0.495 ps	941 fs
Figures 8(c) and 8(c1)	19.90 nm	1574.03; 1593.93 nm	5.4; 5.0 nm	0.513 ps	895 fs
Figures 8(d) and 8(d1)	14.55 nm	1575.94; 1590.49 nm	5.2; 4.8 nm	0.552 ps	944 fs
Figures 8(e) and 8(e1)	~11 nm	~1578; ~1589 nm	NA	NA	348 fs

[a]F. N., figure number corresponding to the detailed characteristics; S. S., spectral spacing of the two solitons; C. W., central wavelength of the two solitons; B. W., 3-dB bandwidth of the two solitons; M. P., modulation period of the autocorrelation trace; P. W., pulse width assumed by a sech^2 pulse profile without considering the unique envelope; NA, the data cannot be described.

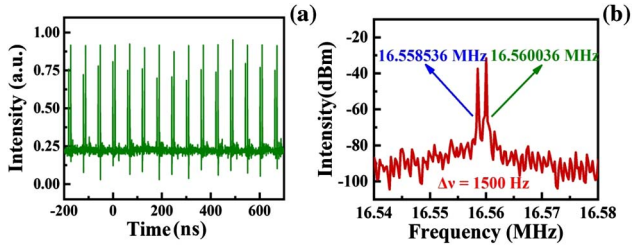

Fig. 9. (a) Pulse train of the dual-wavelength; (b) corresponding RF spectrum.

by slightly adjusting the loss from 0 to 0.4 dB. The 3-dB bandwidths of the dual wavelength show no significant change in the tuning process, as shown in Table 1. Figures 8(a1)–8(e1) provide the corresponding autocorrelation traces and the dual solitons maintain coherent characteristics. The modulation period is tuned from 0.442 to 0.552 ps as the corresponding spectral spacing decreases. It can be seen that the modulation period is reversely related to the spectral spacing, which is verified by the following formula $\Delta\lambda \cdot \Delta\tau = C$, where $\Delta\lambda$ refers to the spectral spacing of the two peaks, $\Delta\tau$ is the modulation period of the soliton, and C is a constant. Assuming a sech^2 pulse profile without considering the unique envelope,

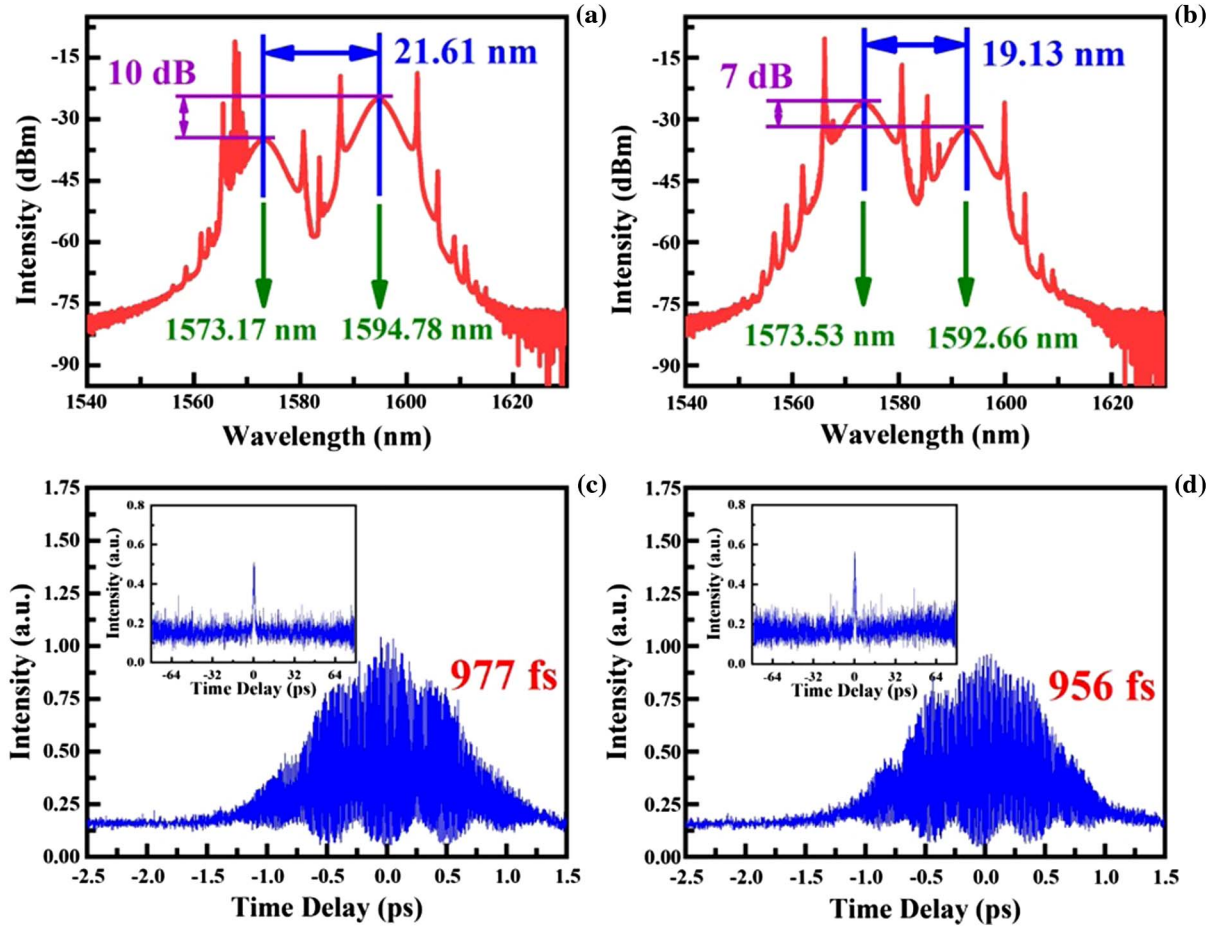

Fig. 10. Controllable pulse energies of the dual wavelength. (a), (b) The spectra; (c), (d) corresponding autocorrelation traces; insets: wide-range autocorrelation trace diagram.

the actual pulse widths have the similar durations around ~900 fs, which is slightly larger than the single-pulse width. It should be noted that when the spectral spacing is small enough, the two mode-locking spectra overlap, and super-broad trapezoid-form spectrum can be obtained, as shown in Fig. 8(e). There are two small peaks near 1578 and 1689 nm, respectively, and the existence of the Kelly sidebands observed in the profile of the spectrum proves that the laser can be considered in dual-wavelength mode-locking operation.

Figure 9 presents the oscilloscope trace and the RF spectrum corresponding to the dual-wavelength soliton shown in Fig. 8(a). It can be obviously observed from Fig. 9(a) that there are two independent pulse sequences. Actually, when one pulse train is stabilized by using the trigger function, the other flows randomly on the oscilloscope screen, indicating that two pulse trains have different group velocities within the fiber ring cavity. However, due to the relatively low scanning frequency of the autocorrelator, the autocorrelation traces do not vary in real time in response to the change in the time separation. The RF spectrum is displayed in Fig. 9(b), where the pulse at 1569.63 nm has a repetition rate of 16.558536 MHz, and the pulse at 1602.64 nm has a repetition rate of 16.560036 MHz. Thus, the repetition rates of the pulse trains at two wavelengths are slightly different, with an approximate interval of 1.5 kHz. This slight difference is caused by the different refractive indices at different wavelengths that are introduced by the group velocity dispersion in the resonant cavity. It can also be seen that the RF peak at 16.560036 MHz is higher than that at 16.558536 MHz, which indicates that the mode-locking pulses at 1602.64 nm have better stability. We believe that the reason for this phenomenon is due to the fact that the pulses at 1569.63 nm with larger pulse energy experience stronger nonlinear accumulation, which finally decreases pulse stability.

In addition, the pulse energy proportion of the dual wavelength can also be continuously changed by slightly tuning the orientation of the PC. Figure 10 shows that the pulse energy of the two peaks in the spectrum can be switched between the dual wavelengths, while the two central peaks are fixed at around 1573 and 1593 nm, and the actual pulse width stays at around 960 fs. The envelope of the autocorrelation trace indicates that the interference phenomenon can still be observed even when the two solitons have different peak energies. However, the intensity of interference is much weaker than that shown in Fig. 8, which means that similar pulse energy is an important condition for the formation of the mutual coherent dual-wavelength solitons.

3. CONCLUSION

In conclusion, a wavelength-tunable and coherent dual-wavelength mode-locking operation is realized in an all-fiber EDF laser using a hybrid NCF-GIMF structure-based SA. By increasing the additional intracavity loss using a VOA, a widely tunable wavelength ranging from 1602.6 to 1555.9 nm with stable single pulses is generated. The solitons centered at different wavelengths have similar spectral FWHM of around 5 nm and a pulse width of around 850 fs. Compared with the other tuning method, the method of cavity loss control possesses the advantages of simple configuration, fast response, no change on the spectral profile, and no intracavity birefringence adjustment. By the proper adjustment of the PC, the dual-wavelength mode-locking operation can be realized, and the separation of the dual spectra can be continuously tuned from 11 to 33.01 nm by changing the additional loss. Besides, a unique amplitude interference envelope in the autocorrelation trace is observed in a dual-wavelength passively mode-locked fiber laser for the first time, indicating the mutual coherence of the dual-wavelength solitons. The approach of coherent solitons offers new possibilities for fundamental research as well as for applications in dual-comb frequency, multicolor pulses in nonlinear microscopy, and so on.

Funding. National Natural Science Foundation of China (NSFC) (61805225, 11804323).

REFERENCES

1. G. Wang, H. Lu, X. Liu, D. Mao, and L. Duan, "Tunable multi-channel wavelength demultiplexer based on MIM plasmonic nanodisk resonators at telecommunication regime," Opt. Express **19**, 3513–3518 (2011).
2. S. Diaz, A. B. Socorro, R. M. Manuel, R. Fernandez, and I. Monasterio, "Stable multi-wavelength fiber lasers for temperature measurements using an optical loop mirror," Appl. Opt. **55**, 8385–8389 (2016).
3. M.-T. Tsai, D.-R. Li, and M.-C. Chan, "Non-invasive image-guided laser microsurgery by a dual-wavelength fiber laser and an integrated fiber-optic multi-modal system," Opt. Lett. **41**, 4847–4850 (2016).
4. I. A. Litago, D. Leandro, M. Á. Quintela, R. A. Pérez-Herrera, M. López-Amo, and J. M. López-Higuera, "Tunable SESAM-based mode-locked soliton fiber laser in linear cavity by axial-strain applied to an FBG," J. Lightwave Technol. **35**, 5003–5009 (2017).
5. H. Ahmad, F. D. Muhammad, M. Z. Zulkifli, and S. W. Harun, "Graphene-based mode-locked spectrum-tunable fiber laser using Mach-Zehnder filter," IEEE Photon. J. **5**, 1501709 (2013).
6. B. Sun, J. Luo, Z. Yan, K. Liu, J. Ji, Y. Zhang, Q. Wang, and X. Yu, "1867–2010 nm tunable femtosecond thulium doped all-fiber laser," Opt. Express **25**, 8997–9002 (2017).
7. X. Zhu, J. Geng, L. Jin, J. Cao, Y. Ji, L. Zou, C. Xu, and G. Zhang, "Widely tunable multi-wavelength passively mode-locked Yb-doped fiber laser operation in an all-normal-dispersion regime," Optik **176**, 496–501 (2019).
8. T. Noronen, O. Okhotnikov, and R. Gumenyuk, "Electronically tunable thulium-holmium mode-locked fiber laser for the 1700–1800 nm wavelength band," Opt. Express **24**, 14703–14708 (2016).
9. J. Kang, C. Kong, P. Feng, X. Wei, Z. Luo, E. Y. Lam, and K. K. Y. Wong, "Broadband high-energy all-fiber laser at 1.6 μm," IEEE Photon. Technol. Lett. **30**, 311–314 (2018).
10. H. Zhang, D. Y. Tang, L. M. Zhao, Q. L. Bao, K. P. Loh, B. Lin, and S. C. Tjin, "Compact graphene mode-locked wavelength-tunable erbium-doped fiber lasers: from all anomalous dispersion to all normal dispersion," Laser Phys. Lett. **7**, 591–596 (2010).
11. Y. Meng, M. Salhi, A. Niang, K. Guesmi, G. Semaan, and F. Sanchez, "Mode-locked Er:Yb-doped double-clad fiber laser with 75-nm tuning range," Opt. Lett. **40**, 1153–1156 (2015).
12. X. Zhao, Z. Zheng, L. Liu, Y. Liu, Y. Jiang, X. Yang, and J. Zhu, "Switchable, dual-wavelength passively mode-locked ultrafast fiber laser based on a single-wall carbon nanotube mode locker and intracavity loss tuning," Opt. Express **19**, 1168–1173 (2011).
13. P. Franco, M. Midrio, A. Tozzato, M. Romagnoli, and F. Fontana, "Characterization and optimization criteria for filterless erbium-doped fiber lasers," J. Opt. Soc. Am. B **11**, 1090–1097 (1994).
14. M. Durán-Sánchez, R. I. Álvarez-Tamayo, B. Posada-Ramírez, B. Ibarra-Escamilla, E. A. Kuzin, J. L. Cruz, and M. V. Andrés, "Tunable dual-wavelength thulium-doped fiber laser based on FBGs and a Hi-Bi FOLM," IEEE Photon. Technol. Lett. **29**, 1820–1823 (2017).

15. S. A. Babin, E. V. Podivilov, D. S. Kharenko, A. E. Bednyakova, M. P. Fedoruk, V. L. Kalashnikov, and A. Apolonski, "Multicolour nonlinearly bound chirped dissipative solitons," Nat. Commun. **5**, 4653 (2014).
16. D. S. Kharenko, A. E. Bednyakova, E. V. Podivilov, M. P. Fedoruk, A. Apolonski, and S. A. Babin, "Cascaded generation of coherent Raman dissipative solitons," Opt. Lett. **41**, 175–178 (2016).
17. Y. Meng, Y. Li, Y. Xu, and F. Wang, "Carbon nanotube mode-locked thulium fiber laser with 200 nm tuning range," Sci. Rep. **7**, 45109 (2017).
18. D. Li, H. Jussila, Y. Wang, G. Hu, T. Albrow-Owen, R. C. T. Howe, Z. Ren, J. Bai, T. Hasan, and Z. Sun, "Wavelength and pulse duration tunable ultrafast fiber laser mode locked with carbon nanotubes," Sci. Rep. **8**, 2738 (2018).
19. K. Guesmi, Y. Meng, A. Niang, P. Mouchel, M. Salhi, F. Bahloul, R. Attia, and F. Sanchez, "1.6 μm emission based on linear loss control in an Er:Yb doped double-clad fiber laser," Opt. Lett. **39**, 6383–6386 (2014).
20. M. Wang, Y. J. Huang, J. W. Yang, Y. Zhang, and S. C. Ruan, "Multi-wavelength mode-locked thulium-doped fiber laser based on a fiber-optic Fabry-Perot interferometer and a nonlinear optical loop mirror," Laser Phys. Lett. **15**, 085110 (2018).
21. H. Zhang, D. Y. Tang, X. Wu, and L. M. Zhao, "Multi-wavelength dissipative soliton operation of an erbium-doped fiber laser," Opt. Express **17**, 12692–12697 (2009).
22. Y. Chen, S. Chen, J. Liu, Y. Gao, and W. Zhang, "Sub-300 femtosecond soliton tunable fiber laser with all-anomalous dispersion passively mode locked by black phosphorus," Opt. Express **24**, 13316–13324 (2016).
23. X. Li, J. Qian, R. Zhao, F. Wang, and Z. Wang, "Dual-wavelength mode-locked fiber laser based on tungsten disulfide saturable absorber," Laser Phys. **27**, 125802 (2017).
24. Z. Wang, D. N. Wang, F. Yang, L. Li, C. Zhao, B. Xu, S. Jin, S. Cao, and Z. Fang, "Er-doped mode-locked fiber laser with a hybrid structure of a step-index-graded-index multimode fiber as the saturable absorber," J. Lightwave Technol. **35**, 5280–5285 (2017).
25. Z. Wang, D. N. Wang, F. Yang, L. Li, C. Zhao, B. Xu, S. Jin, S. Cao, and Z. Fang, "Stretched graded-index multimode optical fiber as a saturable absorber for erbium-doped fiber laser mode locking," Opt. Lett. **43**, 2078–2081 (2018).
26. F. Yang, D. N. Wang, Z. Wang, L. Li, C. Zhao, B. Xu, S. Jin, S. Cao, and Z. Fang, "Saturable absorber based on a single mode fiber–graded index fiber–single mode fiber structure with inner micro-cavity," Opt. Express **26**, 927–934 (2017).
27. T. Chen, Q. Zhang, Y. Zhang, X. Li, H. Zhang, and W. Xia, "All-fiber passively mode-locked laser using nonlinear multimode interference of step-index multimode fiber," Photon. Res. **6**, 1033–1039 (2018).
28. T. Zhu, Z. Wang, D. N. Wang, F. Yang, and L. Li, "Observation of controllable tightly and loosely bound solitons with an all-fiber saturable absorber," Photon. Res. **7**, 61–68 (2019).
29. F. Zhao, Y. Wang, H. Wang, Z. Yan, X. Hu, W. Zhang, T. Zhang, and K. Zhou, "Ultrafast soliton and stretched pulse switchable mode-locked fiber laser with hybrid structure of multimode fiber based saturable absorber," Sci. Rep. **8**, 16369 (2018).
30. T. Ugur and O. Bulend, "All-fiber all-normal-dispersion femtosecond laser with a nonlinear multimodal interference-based saturable absorber," Opt. Lett. **43**, 1611–1614 (2018).
31. J. F. Massicott, J. R. Armitage, R. Wyatt, B. J. Ainslie, and S. P. Craig-Ryan, "High gain, broadband, 1.6 μm Er^{3+}-doped silica fibre amplifier," Electron. Lett. **26**, 1645–1646 (1990).